

THERMAL EMISSION OF WASP-14b REVEALED WITH THREE *SPITZER* ECLIPSES

JASMINA BLECIC AND JOSEPH HARRINGTON

Planetary Sciences Group, Department of Physics, University of Central Florida  
Orlando, FL 32816-2385

NIKKU MADHUSUDHAN

Department Astrophysical Sciences, Princeton University, Princeton, NJ 08544, USA

KEVIN B. STEVENSON, RYAN A. HARDY, CHRISTOPHER J. CAMPO, WILLIAM C. BOWMAN, SARAH NYMEYER, PATRICIO CUBILLOS

Planetary Sciences Group, Department of Physics, University of Central Florida  
Orlando, FL 32816-2385

DAVID R. ANDERSON

Astrophysics Group, Keele University, Keele, Staffordshire ST5 5BG

Submitted to ApJ, November 8, 2011 15:26

## ABSTRACT

WASP-14b belongs to a class of highly irradiated hot Jupiters ( $T_{\text{eq}} = 1866 \text{ K}$ ) with a mass of  $7.3 \pm 0.5 M_J$  and a radius of  $1.28 \pm 0.08 R_J$ . With a mean density of  $4.6 \text{ g cm}^{-3}$ , this transiting planet is one of the densest known to date (Joshi et al. 2009), for planets with periods less than 3 days. We present analytic light-curve models for three *Spitzer* secondary eclipses, Keplerian orbital model, estimates of infrared brightness temperatures, and constraints on atmospheric composition and thermal structure. Although extremely irradiated, WASP-14b does not show any distinctive evidence of a thermal inversion, based on existing observations. In addition, the observations indicate low day-night redistribution ( $f_r < 0.25$ ) and are consistent with chemical compositions at nearly solar abundances. We confirm a significant eccentricity of  $e = 0.087 \pm 0.002$  and refine other orbital parameters.

*Subject headings:* eclipses — planetary systems — planets and satellites: atmospheres — planets and satellites: individual (WASP-14b) — techniques: photometric

## 1. INTRODUCTION

The *Spitzer Space Telescope* (Werner et al. 2004) is the most widely used facility for characterizing extra solar planets. Out of space telescopes, *Spitzer* systematics are among less complex and are very well-studied and modeled, providing an invaluable resource for accurate exoplanet characterization (Seager & Deming 2010). This has enabled the measurement of tens of atmospheres, using the detection of primary and secondary eclipses as the most prolific method of investigation to date.

The planet-to-star flux ratio is enhanced in the infrared due to the planet thermal emission and simultaneous drop in the stellar emission, enabling high-precision photometric measurements. Combining several secondary-eclipse observations measured in broad *Spitzer* bandpasses with the Infrared Array Camera (IRAC, Fazio et al. 2004), a low-resolution dayside spectrum from the planet can be reconstructed, revealing key atmospheric and physical parameters. These measurements can further be used to constrain atmospheric composition, thermal structure, and ultimately the formation and evolution of the observed planet. WASP-14b represents an intriguing object for such an analysis, having characteristics not so common for close-in, highly irradiated giant planets.

WASP-14b (Joshi et al. 2009) was discovered as a part of the SuperWASP survey (Wide-Angle Search for Planets, Polacco et al. 2006; Collier Cameron et al. 2006, 2007). Photometric and radial velocity observations revealed a planetary

mass of  $7.3 \pm 0.5 M_J$  and a radius of  $1.28 \pm 0.08 R_J$ . Its density ( $\rho = 4.6 \text{ g cm}^{-3}$ ) is significantly high compared to typical hot Jupiter densities of  $0.34\text{--}1.34 \text{ g cm}^{-3}$  (Loeillet et al. 2008a). The planet is also very close to its star (semi-major axis  $0.036 \pm 0.001 \text{ AU}$ ), and has a significant orbital eccentricity of  $0.087 \pm 0.002$  (this work).

Detailed spectroscopic analyses of the stellar atmosphere determined that the star belongs to the F5 main-sequence spectral type with a temperature of  $6475 \pm 100 \text{ K}$  and high lithium abundance of  $\log N(\text{Li}) = 2.84 \pm 0.05$ . F-type stars with this temperature should have depleted Li, being close to the Li gap or ‘Boesgaard gap’ (Boesgaard & Tripicco 1986; Balachandran 1995). However, the high amount of Li and a relatively high rotational speed of  $v \sin(i) = 4.9 \pm 1.0 \text{ km s}^{-1}$  indicate that WASP-14 is a young star. Comparing these results with models by Fortney et al. (2007) for the range of planetary masses and radii led Joshi et al. (2009) to constrain the age of the system to  $0.5\text{--}1.0 \text{ Gyr}$ .

Joshi et al. (2009) also discuss the high eccentricity of the planet. Because WASP-14b has a very small orbital distance, probable scenarios for such a significant eccentricity would be either that system age is comparable to the tidal circularization time scale or there is a perturbing body.

Husnoo et al. (2011) performed long-term radial velocity measurements with a goal of discovering or rejecting the presence of a third body. They refine the orbital eccentricity value ( $e = 0.088 \pm 0.003$ ) and spin-orbit angle. They argue that this planet has undergone some degree of orbital evolution, but it is still subject to strong tidal forces. This establishes a new

lower limit for the semimajor axis at which orbital eccentricity can survive tidal evolution for the age of the system. They state that since there is no observable unambiguous trend in residuals with time, there is no firm evidence for an existing planetary companion.

Using the *Spitzer Space Telescope*, we observed three secondary eclipses at 3.6  $\mu\text{m}$ , 4.5  $\mu\text{m}$ , and 8.0  $\mu\text{m}$ . We present analytic light-curve models that incorporate corrections for systematic effects with a new approach to removing them with the Stevenson et al. (2011) pixel sensitivity mapping technique, a Keplerian orbital model, estimates of infrared brightness temperatures, and constraints on atmospheric composition and thermal structure.

In Section 2 we describe our observations. Section 3 discusses data reduction procedures. Section 4 presents our photometry and Section 5 discusses the modeling techniques and results of each dataset. Section 6 presents constraints on the orbit of WASP-14b, and Section 7 reveals the atmospheric structure and composition. In Section 8 we discuss our results and in Section 9 we present our conclusions.

## 2. OBSERVATIONS

The *Spitzer* IRAC instrument observed two events; one at 3.6  $\mu\text{m}$  in 2010 March (Knutson’s program 60021) and one simultaneous observation in two wavelength bands (4.5 and 8.0  $\mu\text{m}$ ) in 2009 March (Harrington’s program 50517). Observation at 3.6  $\mu\text{m}$  (channel 1) was made in subarray mode with 2 s exposure, while observations at 4.5 and 8.0  $\mu\text{m}$  (channels 2 and 4) were made in stellar mode ( $2 \times 2/12$ ) with pairs of 2 s frames taken in the 4.5  $\mu\text{m}$  band for each 12 s frame in the 8.0  $\mu\text{m}$  band. This mode was used to avoid saturation in channel 2.

TABLE 1  
OBSERVATION INFORMATION

Channel	Observation Date	Start Time [JD]	Duration [s]	Exposure Time [s]	Number of Frames
Main Science Observation					
Ch1	2010-03-18	2455274.4707	28055.4	2	215
Ch2	2009-03-18	2454908.8139	19998.7	$2 \times 2$	2982
Ch4	2009-03-18	2454908.8139	19998.7	12	1481
Pre-observation					
Ch2+4	2009-03-18	2454908.7877	2019	2	213
Post-observation					
Ch2+4	2009-03-18	2454909.0455	367	$2 \times 2, 12$	10

We have pre- and post-calibration frames for the 4.5 and 8.0  $\mu\text{m}$  observation. Prior to the main observation, we exposed the array to a relatively bright source. That quickly caused the saturation of the detector, and produced less-steep increase during the main observation (Section 5.2). During the short post-eclipse observation, frames of the blank sky allowed us to check and demonstrate that there are no warm pixels in the aperture. The *Spitzer* pipeline version used for 3.6  $\mu\text{m}$  observation is S18.14.0 and for 4.8 and 8.0  $\mu\text{m}$  observation is S18.7.0. The start date of each observation, duration, exposure time and total number of frames are given in Table 1.

## 3. DATA REDUCTION

### 3.1. Background

Our analysis performs Photometry for Orbits, Eclipses and Transits (POET). It produced light curves from *Spitzer* Basic Calibrated Data Frames (BCD), fits models to the light curves,

and assesses uncertainties. The derived parameters constrain a separate orbital and atmospheric model. In this section we give a general overview of POET’s routines. The following sections will explain in detail those relevant for our analysis.

Each analysis starts with identifying and flagging bad pixels in addition to the ones determined by the *Spitzer* bad pixel mask (see Section 4). Then we perform centering. Due to the  $\sim 0.1\%$  relative flux level of secondary-eclipse observations and *Spitzer*’s relative photometric accuracy of 2% (Fazio et al. 2004), we apply a variety of centering routines, looking for the most accurate one. Three methods are used to determine the PSF center precisely: center of light, two-dimensional Gaussian fitting, and least asymmetry (see Lust et al. 2012). We then apply  $5 \times$ -interpolated aperture photometry (Harrington et al. 2007), where each image is re-sampled using bilinear interpolation. This allows the inclusion of partial pixels, thus reducing pixellation noise (Stevenson et al. 2011). We subtract the background within a specified annulus centered on the star, and during testing of the large range of aperture sizes, we discard the frames with bad pixels in the photometry aperture.

To explore the parameter space and estimate uncertainties, we use our Markov Chain Monte Carlo routine (MCMC, see Section 3.3), where we model all known systematics and the eclipse event simultaneously, using at least  $10^6$  iterations (Stevenson et al. 2010; Campo et al. 2011). To test adequate sampling, we ran four independent MCMC chains. To ensure the convergence of all chains, we run as many iterations as necessary until the Gelman & Rubin (1992) test for all free parameters drop below 1%. Our MCMC routine can model events separately or simultaneously, sharing parameters such as the eclipse midpoint, ingress/egress times or duration.

To find the best model, we test all systematic models known in the literature and some of our own. We use our newly developed (Stevenson et al. 2011) BiLinearly-Interpolated Subpixel Sensitivity (BLISS) technique to model intrapixel sensitivity variation at the sub-pixel level (see Section 3.2). Using both bilinear (BLI) and nearest-neighbor (NNI) interpolation and over 1000 knots (the control points), we map the pixel surface. This method does not require any free parameters and quickly converges.

To determine the best aperture size, we choose the solution with the smallest standard deviation of normalized residuals (SDNR). The best model for a given aperture size is determined by applying the Bayesian (BIC) and Akaike (AIC) information criteria, which compare models with different numbers of free parameters (see Section 3.3).

We also base our decision upon the level of correlation in the residuals (Campo et al. 2011; Nymeyer et al. 2011). Less-correlated models are better, if there is no significant difference in AIC and BIC (see Sections 3.3 and 5.1).

Finally, we report Julian Date mid-times in both  $\text{BJD}_{\text{UTC}}$  (Coordinated Universal Time) and  $\text{BJD}_{\text{TT}}$  ( $\text{BJD}_{\text{TDB}}$ , Barycentric Dynamical Time), calculated using the Jet Propulsion Laboratory (JPL) Horizons system, to facilitate handling discontinuities due to leap seconds and to allow other researchers to compare mid-times of the eclipses easily.

### 3.2. Modeling Systematics

Modeling systematics is critical to accurate atmospheric characterization. So far, there are two major discrepancies presented in the literature. Tinetti et al. (2007) find a deeper transit of HD189733b than Désert et al. (2009), which indicates a larger optical depth and the presence of water va-

por higher in the atmosphere. Knutson et al. (2009b), re-analyzing 8.0  $\mu\text{m}$  observations of HD149026b, by applying a different set of systematic models, find a range of eclipse depths from 0.05 - 0.09%, preferring the lower values as their best. This value is half that of Harrington et al. (2007) (see Stevenson et al. (2011), for our latest analyses of this data set). To avoid similar and future errors, our team is heavily focused on modeling systematics, testing all of the known analytic model components.

*Spitzer's* IRAC has four broad photometric bandpasses: 3.6, 4.5, 5.8, and 8.0  $\mu\text{m}$  (channels 1, 2, 3 and 4). All four channels exhibit large systematic errors on the scale of our requirements. The 3.6 and 4.5  $\mu\text{m}$  bands use InSb detectors, and the 5.8 and 8.0  $\mu\text{m}$  bands Si:As detectors. InSb detectors are known to show variable response in quantum efficiency depending on the centroid location within the pixel. This intrapixel sensitivity is greatest at pixel center and declines toward the edges of the pixel, typically by several percent (Morales-Calderón et al. 2006). It is also not symmetric about the center of the pixel and the amplitude of the effect varies from pixel to pixel. Over the total duration of the observation, the position varies by several tenths of the pixel width and since the motion of the stellar center goes through this region frequently, this systematic is adequately sampled during a single eclipse observation. One minimizes this effect by observing with fixed pointing (Reach et al. 2005; Charbonneau et al. 2005; Harrington et al. 2007; Stevenson et al. 2010).

The other systematic, the most prominent and well studied, is the time varying sensitivity, called the *ramp* effect. This is a baseline effect which may affect all the channels, but is most pronounced at 8.0  $\mu\text{m}$  (Charbonneau et al. 2005; Harrington et al. 2007). It is observed as apparent increase in flux with time, which is believed to be caused by charge trapping. An eclipse is superimposed on this baseline and is easily separated, but not without adding uncertainty to the eclipse depth. After many hours of observations this effect reaches a plateau, hence a way to stabilize it is to point the array to a bright source prior to the main observation. This causes saturation and consequently produce a flatter ramp (Knutson et al. 2009b; Seager & Deming 2009). The systematic is particularly important for weak eclipses, where an incorrect choice of ramp can produce an incorrect eclipse depth.

Although each type of systematic, due to different type of alloy on the detectors, is strong in different set of channels (ramp effect channels 3 and 4, intrapixel effect, channels 1 and 2), it was recently reported that both systematics were seen in other channels (Stevenson et al. 2010). That is why we model all variations in all channels.

To model ramp effect, we use different forms of exponential, logarithmic, and polynomial models used in the literature, and some of our own, from more than 10 different equations implemented in our pipeline (see the full set of equations in Stevenson et al. 2011). For each channel we test all ramp models, assessing the best one by using criteria listed at the end of Section 3.3.

Intrapixel variability, which may vary up to 3.5% within the pixel, is modeled with our new intrapixel technique, called BLISS mapping (Stevenson et al. 2011). This technique, opposed to the widely used two-dimensional polynomial fitting (Knutson et al. 2008; Machalek et al. 2009; Fressin et al. 2010) and the mapping technique developed by Ballard et al. (2010), maps the spatial variability on a subpixel-scale grid using bilinear interpolation, and shows significant improvement in both SDNR and BIC compared to other methods. See

Stevenson et al. (2011) for comparison tests.

This method first divides the observed flux by eclipse and ramp models, assuming that any residual fluxes are related to the pixel position. Then it creates a rectangular  $xy$  grid of knots at subpixel resolution, which are used as control points in the interpolation. The flux value of a particular knot is the mean of the residual fluxes assigned to that knot.

We use over 1000 knots to map the pixel surface and two interpolation calculations, bilinear (BLI) and nearest-neighbor (NNI), to generate the sensitivity map (see Section 5.1). Nearest-neighbor assigns each point the value of its nearest knot, and does not consider the values of neighboring points, producing a piecewise-constant interpolant. See Stevenson et al. (2011) for more detail about this technique.

The crucial part in this analysis is determining the knot spacing (bin size), which gives resolution in the position space. The bin size must be small enough to catch any small-scale variation, but also large enough to ensure no correlation with the eclipse fit (see Section 5.1). Assuming accurate centering, BLI should always outperform NNI. The bin size where NNI outperforms BLI is indication of the centering precision, and determines the bin size for the particular data set. If NNI always outperforms BLI, that is the indication that intrapixel variability is very weak and intrapixel modeling is unnecessary.

### 3.3. Modeling Light Curves and the Best Fit Criteria

To find the best model, for each aperture size we systematically explore every combination of ramp model and intrapixel sensitivity model. The final light curve model is expressed as,

$$F(x,y,t) = F_s R(t) M(x,y) E(t), \quad (1)$$

where  $F(x,y,t)$  is the aperture photometry flux,  $F_s$  is the constant system flux outside of the eclipse,  $R(t)$  is time-dependent ramp model,  $M(x,y)$  is the position-dependent intrapixel model and  $E(t)$  is the eclipse model (Mandel & Agol 2002).

To estimate uncertainties we use our MCMC routine with the Metropolis-Hastings random walk algorithm with at least  $10^6$  iterations, to ensure accuracy of the result. This routine simultaneously applies eclipse parameters and *Spitzer* systematics, exploring the parameter phase space, determining uncertainties and correlations between the parameters. It leaves depth, duration, midpoint, system flux, and ramp parameters free. Additionally, the routine can model multiple events at once, sharing the eclipse duration, midpoint and ingress/egress times. These joint fits are particularly appropriate for channels observed together (see Campo et al. 2011 for more details about our MCMC routine).

To avoid fixing any model parameter during MCMC, we use the Bayesian prior (Gelman 2002). This is particularly relevant for noisy or low S/N datasets where some parameters are not well constrained by the observations, as is the case for ingress and egress times. For them we use informative priors, taken from the literature.

Photometric uncertainties used in our analyses are derived by fitting an initial model with a  $\chi^2$  minimizer and re-scaling it to reduced  $\chi^2$  of 1, since *Spitzer* pipeline uncertainties are generally over-estimated (Harrington et al. 2007). This scaling factor is proportional to SDNR of the models. Upon rescaling, we re-run the least-squared minimizer with the new uncertainties, and then MCMC. If MCMC finds a lower  $\chi^2$

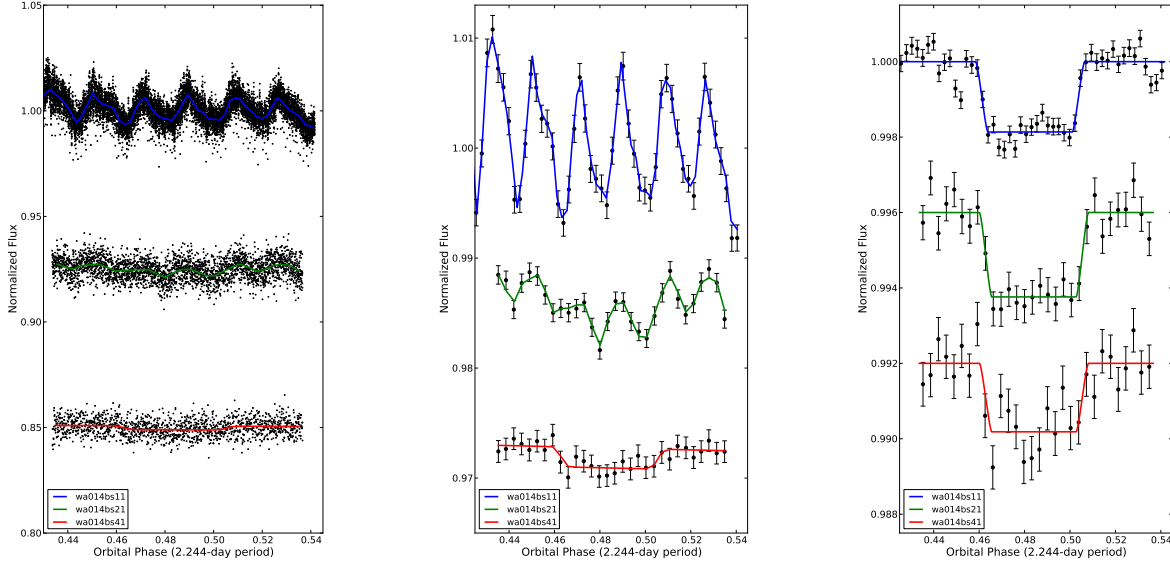


FIG. 1.— Raw (left), binned (center) and systematics-corrected (right) primary transit light curves of WASP-14b at 3.6, 4.5 and 8.0  $\mu\text{m}$ . The results are normalized to the system flux and shifted vertically for the purpose of comparison. The colored lines are best-fit models, the black curves omit their transit models, and the error bars are  $1\sigma$  uncertainties. As seen in the binned plots of wa014bs21, wa014bs41, a linear function accurately fits the time-dependent systematic without the need to clip any initial data points. wa014bs11 fits better if initial data points are clipped (see Section 5.1).

value than the minimizer, we re-run the minimizer starting from the MCMC’s best value. The minimizer will find an even better  $\chi^2$ . We then restart the MCMC from the new minimizer solution, and run  $10^6$  iterations to derive uncertainties for each of the parameters (Campo *et al.* 2011)

Our measures of goodness of fit are SDNR, BIC and AIC values (Liddle 2007):

$$\text{BIC} = \chi^2 + k \ln N, \quad (2)$$

$$\text{AIC} = \chi^2 + 2k, \quad (3)$$

where  $k$  is the number of free parameters,  $N$  is the number of data points. These criteria penalize additional free parameters in the system, with better fits having lower values. To appropriately compare BIC and AIC values for the same aperture size, and determine the best fit, we use the same uncertainties for each dataset, and model all combinations of ramp models and intrapixel model. SDNR values are used to compare different aperture sizes. The lowest value defines the best aperture size.

Equally important is the correlation in the residuals (see Section 5.1). We plot and compare the theoretical  $1/\sqrt{N}$  scaling with the RMS model residuals *vs.* bin size (Pont *et al.* 2006; Winn *et al.* 2008). If there is no major deviation in those two curves, there is a lack of significant time-dependent photometric noise correlation in the final models.

After MCMC is finished, we study parameter histograms and pairwise correlations plots, making sure that the phase space minimum is global.

#### 4. WASP-14b PHOTOMETRY

For our analyses, we used Basic Calibrated Data (BCD) frames generated in the *Spitzer* IRAC pipeline (Fazio *et al.* 2004). The pipeline version used for each observation is given in Section 2. Our data reduction procedure started with applying *Spitzer*’s bad pixel masks and with our procedure for flagging additional bad pixels (Harrington *et al.* 2007). In each

group of 64 frames and at each pixel position, we applied two-iteration outlier rejection, which calculated the frame median and the standard deviation from the median, and flagged pixels that deviates more than  $4\sigma$ . Then we found the stellar centroid for the photometry, by using a 2D Gaussian fit to data in an aperture radius of four pixels.

Light curves were extracted using  $5 \times$ -interpolated aperture photometry (Harrington *et al.* 2007), for every aperture radius from 2.25 to 4.25 pixels, in 0.25-pixel steps. The background is estimated and subtracted before the photometry, in an annulus centered on the source with inner and outer radii defined in Section 5.4.

To calculate the Barycentric Julian Date (BJD) of each exposure we used the mid-exposure time of each frame, based on the UTCS-OBS value in the FITS header and the frame number. We performed our barycentric light-time correction using our own code and the coordinates of the *Spitzer* spacecraft from the Horizons ephemeris system of the Jet Propulsion Laboratory. The times are corrected to  $\text{BJD}_{\text{TDB}}$  to remove the effects of leap seconds and relativity.

#### 5. WASP-14b SECONDARY ECLIPSES

Here, we discuss each observation in detail, particularly focusing on channel 1, due to the demanding analysis of that data set. In Subsection 5.1 we give our control plots, as an example of how we verify that our results are indeed the best solution for the particular data set. We present each channel separately and then a joint fit. We give our best model fits, with the particular ramp and intrapixel model used for each data set, corresponding eclipse depths and brightness temperatures and joint best-fit eclipse parameters. Figure 1 shows our best fit eclipse light curves. In Appendix we give parameters for the WASP-14 system, derived from this analysis and from the literature.

##### 5.1. Channel 1 - 3.6 $\mu\text{m}$

The observation in channel 1 lasted 7.8 hours, during which a good amount of the system baseline was observed before

and after the secondary eclipse event. Images that are taken at the start of the observation have larger pointing offset, due to the telescope settling prior to the eclipse observation. Discarding starting data in that case improves the fit. Some initial data points ( $\sim 36$  minutes, 1100 of 13760 points) were therefore removed from the fitting procedure. In Figure 2 we compare SDNR values for models with different ramps with and without exclusion of the initial data points. Models with initial data points removed produce better fits with lower values for SDNR.

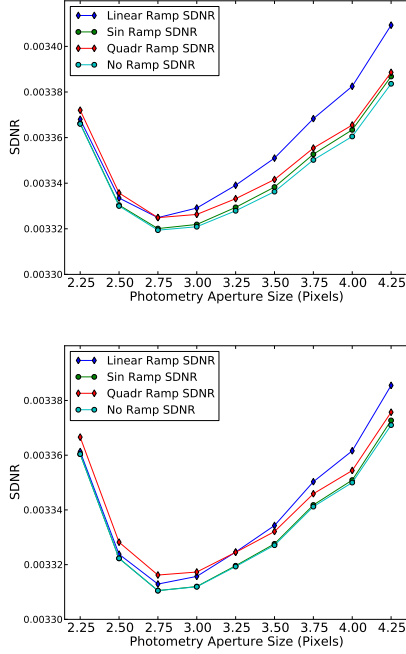


FIG. 2.— **Top:** Channel 1 comparison of different ramp models with all observational points included (*no-preclip*). Plot shows SDNR vs. aperture size. A lower value indicates a better model fit. **Bottom:** Channel 1 comparison of different ramp models with 1100 points excluded (*preclip*).

Starting from the aperture size of 2.25 and continuing with an increment of 0.25-pixel, we tested all of the ramp models (linear, rising, exponential, sinusoidal, double exponential, logarithmic, etc.). Corresponding equations are listed in Stevenson et al. (2011). To determine the best solution we consider our best-fit criteria (see Section 3.3) and study the correlation plots. Most of the models produced obvious bad fits, so minimizer and shorter MCMC runs eliminated them. The best aperture radius is 2.75 pixels (see Figure 2, bottom panel). We tested the dependence of eclipse depth on aperture radius (Anderson et al. 2010). The trend in some events may indicate a slightly imperfect background removal (see Figure 3). The effect is less than  $1\sigma$  on the eclipse depth.

Intrapixel variability is the strongest systematic in *Spitzer* channels 1 and 2. The sensitivity BLISS map is given in Figure 4. The correlation coefficients between eclipse depth and BLISS map knots are given in Figure 5. As we stated in the Section 3.2 the most important variable to consider with BLISS is the bin size. It defines the resolution in position space and gives insight into the average behavior. The position precision for channel 1, measured as RMS of the position difference on consecutive frames, shows significant difference between the  $x$  and  $y$  axes (see Figure 6, upper panel). We considered a range of bin sizes for both BLI and NNI around the

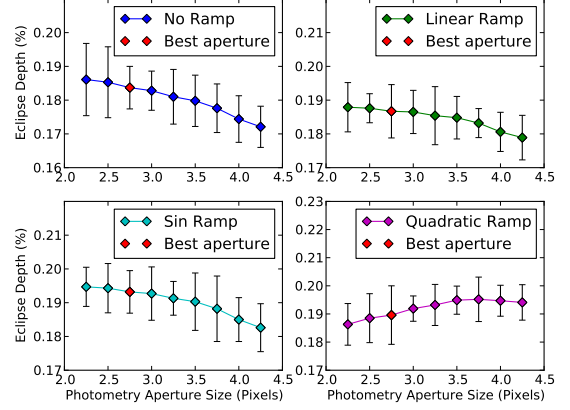


FIG. 3.— The best-fit eclipse depths as a function of photometry aperture size for wa014bs11. All four best ramp models are plotted (see below). The red point indicates the best aperture size for that channel. The eclipse-depth uncertainties are the result of 1000 MCMC iterations. The trend shows insignificant dependence of eclipse depth on aperture size (less than  $1\sigma$ ).

calculated precision. The best bin size for this data set was determined when NNI outperformed BLI. It is 0.004 pixels for  $x$  and 0.01 for  $y$ .

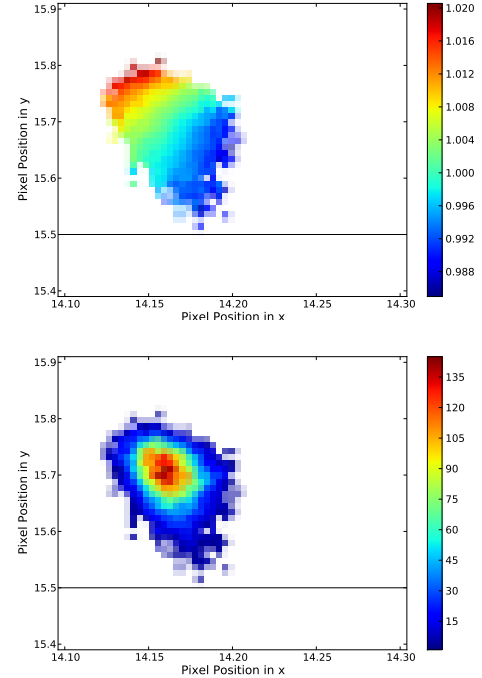


FIG. 4.— **Top:** BiLinearly-Interpolated Subpixel Sensitivity (BLISS) map of wa014bs11. Redder (bluer) colors indicate higher (lower) subpixel sensitivity. The horizontal black lines defines the lower pixel boundary. **Bottom:** Pointing histogram. Colors indicate the number of points in a given bin.

We also tested two-dimensional polynomial intrapixel models (Knutson et al. 2008; Stevenson et al. 2010; Campo et al. 2011):

$$V_{IP}(x, y) = p_1 y^2 + p_2 x^2 + p_3 xy + p_4 y + p_5 x + 1, \quad (4)$$

where  $x$  and  $y$  are the centroid coordinates relative to the pixel center nearest the median position and  $p_1 - p_5$  are free parameters. Both SDNR and BIC show significant improvements with the new BLISS models over the polynomial models (see

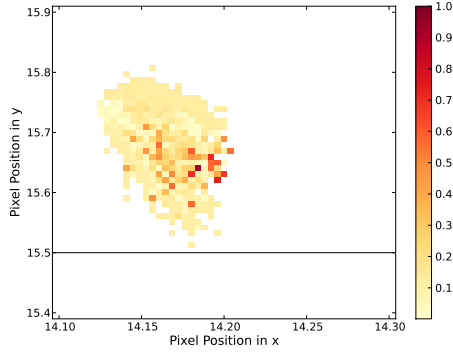


FIG. 5.— Correlation coefficients between eclipse depth and computed BLISS map knots for wa014bs11. The correlation regions (in red) indicate that it is necessary to compute the BLISS map at each step of an MCMC routine, so that we could correctly assess the uncertainty on the eclipse depth.

Table 2. The improvement in BIC is expected, since neither BLI nor NNI require any free parameters. The improvement in SDNR confirms that interpolation offers a better fit to the data (see Stevenson *et al.* 2011 for other tests that compare polynomial and BLISS intrapixel models).

TABLE 2  
COMPARISON BLISS AND BEST POLYNOMIAL MODEL

Ramp Model	BLISS		Polynomial-Quadratic	
	SDNR	BIC	SDNR	BIC
Channel 1				
No ramp	0.003313	12350.0	0.0033853	12593.2
Linear	0.003311	12342.3	0.0033852	12588.5
Sinusoidal	0.003316	12342.2	0.0033855	12590.5
Quadratic	0.003310	12351.5	0.0033850	12597.3
Channel 2				
Linear	0.004472	2971.9	0.0045272	2992.2

In this channel, we detect photometric noise correlations in our models, with consistent residual variation observed in all aperture sizes, with all ramp models, and at every bin size (see Figure 6, bottom panel and Figure 7, left panel). Although channels 1 and 2 (3.6 and 4.5  $\mu\text{m}$ ) both exhibit strong intrapixel variations due to the same material present on the detector (InSb), typically channel 1 exhibits larger sensitivity than channel 2 even if the star is placed in the middle of the pixel (Knutson *et al.* 2011). However, although the star falls close to the edge of the pixel, this time variation is unusually high, and cannot be modeled by any of our position- or time-dependent systematic models. This might indicate that this young, WASP-14 star is still active.

In our work on dozens of eclipses, we have often found the same Spitzer channel to behave differently at different times, even on the same star. Our systematics removal algorithms correct the worst effects, which are consistent, but there is often still some significant baseline scatter or oscillation. While one might expect certain kinds of stars to be relatively stable, recall that Spitzer reaches  $\sigma \sim 0.01\%$  sensitivity in these observations, and stellar oscillations of this scale and at these wavelengths are not well studied. So, it is not fully clear whether these effects come from the observatory or the star. Since scatter and oscillation often persist during an eclipse, and since a change in planetary signal of the magnitude seen would generally mean an unbelievably dramatic change in the planet, we feel justified in treating the scatter or oscillation phenomenologically. If there is significant pointing offset at the start of the observation due to the telescope settling, we

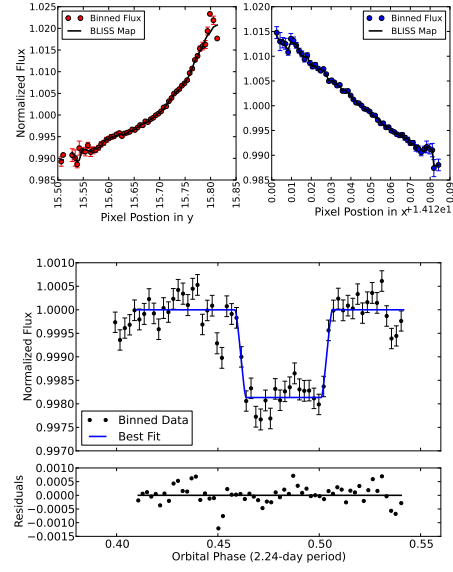


FIG. 6.— **Top:** Projected BLISS map of wa014bs11 integrated along the  $x$  (right) and  $y$  (left) axes. This position dependence variability is effectively fitted with our new BLISS mapping technique. **Bottom:** Residuals for the channel 1 observations (lower panel) display correlated noise both in and out of the eclipse, probably due to stellar activity.

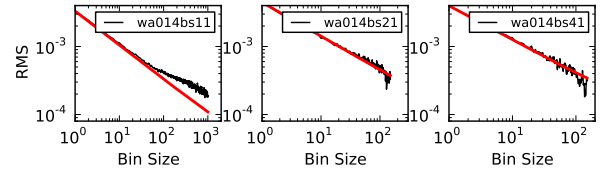


FIG. 7.— Correlations of the residuals for the three secondary eclipses of WASP-14b. Black color represents the RMS residual flux vs. bin size. The red line shows the predicted standard error for Gaussian noise. Large excesses above the red line indicate correlated noise at that bin size (see Section 5.1).

remove it by clipping large excursions and we choose the ramp model that fits best under BIC and AIC. Our MCMC accounts for any correlation between eclipse and model parameters, and our RMS vs. bin size analysis accounts for any residual time correlation of the residuals.

We performed  $10^6$  MCMC iterations to determine the parameter posterior distributions and their uncertainties. We used the Bayesian informative prior for the values of ingress and egress times, obtained from Joshi *et al.* (2009) and David R. Anderson (personal communication, 2010). All other parameters (eclipse midpoint, eclipse duration, eclipse depth, system flux, and ramp parameters) were left free.

TABLE 3  
CHANNEL 1 RAMP MODELS

Ramp Model	SDNR	BIC	Eclipse Depth [%]
No ramp	0.003313	12350.0	$0.1837 \pm 0.0071$
Linear	0.003311	12342.3	$0.1867 \pm 0.0072$
Sinusoidal	0.003316	12342.2	$0.1932 \pm 0.0071$
Quadratic	0.003310	12351.5	$0.1896 \pm 0.0098$

Considering all the above criteria (see also section 3.3), we selected 4 ramp models that produce almost identical SDNR and BIC values. We concluded upon studying output results, histograms and correlation plots that there is no single best solution for this data set. Because quadratic and sinusoidal ramp



models generally produce deeper eclipse depths, for the final atmospheric analyses we selected two extreme final results that will constrain the range of possible temperature-pressure profiles and chemical abundances. The first model does not use a ramp model component and has the lowest value for the eclipse depth and the second model uses the sinusoidal ramp model that has the highest values for the eclipse depth. The SDNR and BIC values with the eclipse depths are given in Table 3.

### 5.2. Channel 2 - 4.5 $\mu\text{m}$

Channel 2 and 4 were observed at the same time. We first modeled each channel separately, determining the best aperture size, time-variability (ramp) model, and bin size for BLISS. Then we applied the joint fit.

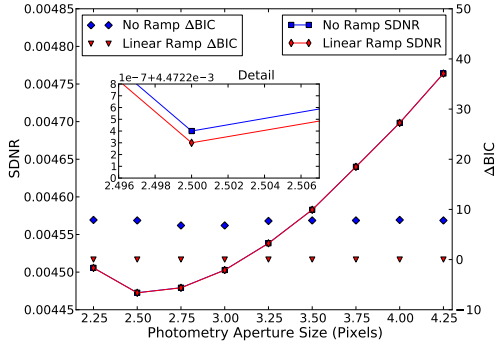


FIG. 8.— Channel 2 comparison between linear and no ramp models. Plot shows SDNR and  $\Delta\text{BIC}$  vs. aperture size. A lower value indicates a better model fit.

The observation in channel 2 lasted 5.5 hours. There was no stabilization period observed in the data, so no points were removed from the analysis. The best aperture radius is 2.50 pixels (see Figure 8). We also test the dependence of eclipse depth on aperture radius (see Figure 9). The eclipse depths are well within  $1\sigma$ .

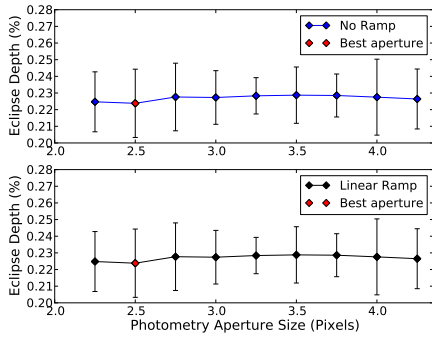


FIG. 9.— The best-fit eclipse depths as a function of photometry aperture size for wa014bs21. The red point indicates the best aperture size for that channel. The eclipse-depth uncertainties are the result of 1000 MCMC iterations. The trend shows insignificant dependence of eclipse depth on aperture size (much less than  $1\sigma$ ).

Prior to the science observations in channels 2 and 4, we observed a 212-frame preflash, exposing the array to a relatively bright source to reduce the time-dependent sensitivity (ramp) effect in channel 4 (Charbonneau et al. 2005; Harrington et al. 2007; Knutson et al. 2008). This produced saturation within the 42 minutes of the observation and led to a smaller rate of increase (see Figure 10).

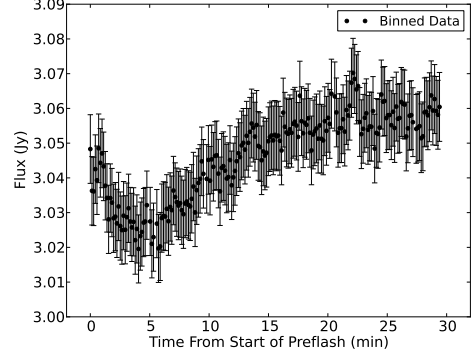


FIG. 10.— Preflash light curve. The preflash source is bright compared to WASP-14b, which ramps array sensitivity before the science observations. Without a preflash, similar observations generally show a steeper and longer ramp.

We tested the full set of ramp equations and discarded obvious bad fits after shorter runs. Among acceptable ones, the lowest BIC value (see Table 4) determined that the final best ramp model is linear (see Eq. 5).

$$R(t) = r_1(t - 0.5) + 1, \quad (5)$$

where  $t$  is orbital phase and  $r_1$  is a free parameter.

TABLE 4  
CHANNEL 2 RAMP MODELS

Ramp Model	SDNR	BIC	Eclipse Depth [%]
No Ramp	0.0044726	2964.2	$0.224 \pm 0.012$
Linear	0.0044725	2971.9	$0.224 \pm 0.018$
Quadratic	0.0044723	2979.9	$0.241 \pm 0.025$
Rising	0.0044726	2980.1	$0.224 \pm 0.021$
Lin+Log	0.0044690	2983.9	$0.228 \pm 0.017$

Each observation ended with a 10-frame, post-eclipse observation of blank sky in the same array position as the science observations to check for warm pixels in the photometric aperture. There were none.

To remove intrapixel variability we again apply our new BLISS technique. We also tested the intrapixel effect with a second-order, two-dimensional polynomial (see Eq. 4), confirming that the BLISS technique gives a better fit (see Table 2). Position precision in the channel 2 is 0.02 pixels for  $x$  and 0.014 pixels for  $y$ . The best bin size is 0.028 pixels in  $x$  and 0.023 pixels in  $y$ . The best aperture size, ramp model, and bin size for the intrapixel variability are then used in our joint fit (see Section 5.4), which gave us the eclipse depths and the brightness temperatures in Section 5.4.

TABLE 5  
CHANNEL 4 RAMP MODELS

Ramp Model	SDNR	BIC	Eclipse Depth [%]
No Ramp	0.0039799	1459.2	$0.181 \pm 0.013$
Linear	0.0039770	1464.3	$0.182 \pm 0.012$
Rising	0.0039799	1466.4	$0.198 \pm 0.030$
Quadratic	0.0039763	1471.3	$0.181 \pm 0.018$
Lin+Log	0.0039799	1481.0	$0.181 \pm 0.024$

### 5.3. Channel 4 - 8.0 $\mu\text{m}$

Again, no stabilization period was observed in this data set, hence no data points were removed from the 8.0  $\mu\text{m}$  dataset.

TABLE 6  
3-JOINT BEST-FIT ECLIPSE LIGHT-CURVE PARAMETERS.

Parameter	Channel 1	Channel 2	Channel 4
Array Position ( $\bar{x}$ , pix)	14.16	23.82	24.6
Array Position ( $\bar{y}$ , pix)	15.69	24.11	21.9
Position Consistency <sup>a</sup> ( $\delta_x$ , pix)	0.005	0.02	0.021
Position Consistency <sup>a</sup> ( $\delta_y$ , pix)	0.012	0.014	0.025
Aperture Size (pix)	2.75	2.5	3.5
Sky Annulus Inner Radius (pix)	8.0	12.0	12.0
Sky Annulus Outer Radius (pix)	20.0	30.0	30.0
System Flux $F_s$ ( $\mu$ Jy)	$102802.0 \pm 4.0$	$66081.0 \pm 8.0$	$24379.0 \pm 4.0$
Eclipse Depth (%)	$0.187 \pm 0.007$	$0.224 \pm 0.018$	$0.182 \pm 0.022$
Brightness Temperature (K)	$2292.0 \pm 40.0$	$2292.0 \pm 97.0$	$1637.0 \pm 120.0$
Eclipse Midpoint (orbits)	$0.4825 \pm 0.0003$	$0.4841 \pm 0.0005$	$0.4841 \pm 0.0005$
Eclipse Midpoint (BJD <sub>UTC</sub> - 2,450,000)	$5274.6609 \pm 0.0007$	$4908.9288 \pm 0.0011$	$4908.9288 \pm 0.0011$
Eclipse Midpoint (BJD <sub>TDB</sub> - 2,450,000)	$5274.6617 \pm 0.0007$	$4908.9296 \pm 0.0011$	$4908.9296 \pm 0.0011$
Eclipse Duration ( $t_{4-1}$ , hrs)	$2.58 \pm 0.03$	$2.58 \pm 0.03$	$2.58 \pm 0.03$
Ingress/Egress Time ( $t_{2-1}$ , hrs)	$0.291 \pm 0.007$	$0.291 \pm 0.007$	$0.291 \pm 0.007$
Ramp Name	linear	linear	linear
Intrapixel Method	BLISS	BLISS	-
Ramp, Linear Term ( $r_1$ )	$0.0044 \pm 0.0010$	$-0.0017 \pm 0.0031$	$-0.005 \pm 0.004$
Minimum Number of Points Per Bin	4	5	-
Total Frames	13760	2982	1491
Frames Used	12308	2944	1433
Rejected Frames (%)	0.486919	0.335345	3.89001
Free Parameters	6	4	3
Number of Data Points in Fit	12308	2944	1433
AIC Value	12313.7	4384.1	4384.1
BIC Value	12358.2	4428.79	4428.79
SDNR	0.00331051	0.0044727	0.00397753
Uncertainty Scaling Factor	0.178797	0.542751	0.585052
Photon-Limited S/N (%)	72.7	90.4	68.1

<sup>a</sup>RMS frame-to-frame position difference.

Since we had the pre-calibration frames for this channel, which made the sensitivity increase more stable and less pronounced, the linear ramp was the best model for the observed time-variability (see Table 5). This is also confirmed with our best fit criteria and the lowest BIC value. No ramp model is excluded because channel 4 is known to exhibit strong ramp effect (Charbonneau et al. 2005; Harrington et al. 2007).

The best aperture size is 3.50 pixels (see Figure 11). We again test for the dependence of eclipse depth with aperture size (see Figure 12).

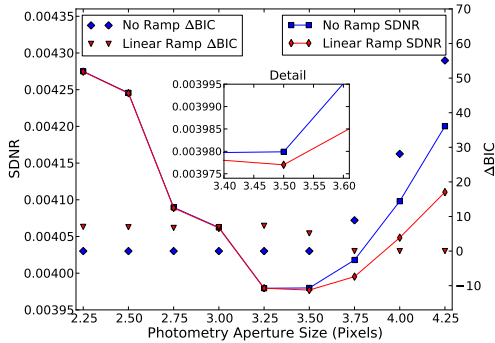


FIG. 11.— Channel 4 comparison between linear and no ramp models. The plot shows SDNR and  $\Delta$ BIC vs. aperture size. A lower value indicates a better model fit.

Even though intrapixel variability is not so strong in the *Spitzer* channels 3 and 4, channel 4 does exhibit a pixellation effect (see Stevenson et al. 2011 and Anderson et al. 2010), which justifies testing whether BLISS can give a better fit. Upon testing a full set of bin sizes, we concluded that NNI

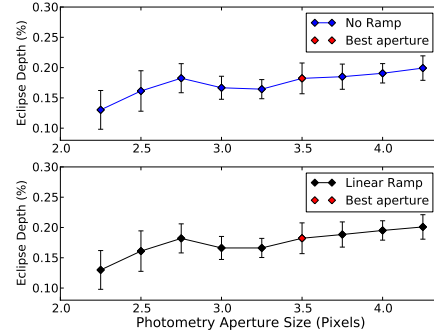


FIG. 12.— The best-fit eclipse depths as a function of photometry aperture size for wa014bs41. The red point indicates the best aperture size for that channel. The eclipse-depth uncertainties are the result of 1000 MCMC iterations. This channel has the lowest S/N ( $\sim 8$ ). The aperture size of 2.25 pixels shows excess noise. Excluding it, the trend exhibits insignificant dependence of eclipse depth on aperture size (less than  $1\sigma$ ).

always outperforms BLI. That is the indication that intrapixel variability is very weak or non existing and can be ignored.

The best aperture size and ramp model are used in our joint fit (see Section 5.4), which gave us the eclipse depths and the brightness temperatures in Section 5.4.

#### 5.4. Joint Fit

To produce final joint-model fits, we run  $10^6$  MCMC iterations for all channels simultaneously, fitting a common eclipse duration for channel 1, 2 and 4, and a common midpoint time for the channels observed together (channel 2 and 4). We again used the informative prior for ingress and egress times (Joshi et al. 2009 and David R. Anderson, personal commu-



TABLE 7  
BEST JOINT-MODEL FITS

Label	Wavelength [ $\mu\text{m}$ ]	Ramp Model	Intrapixel Model	Bin Size in $x$	Bin Size in $y$	Eclipse Depth [%]	Brightness Temp. [K]
wa014bs11	3.6	linear (see also section 5)	BLISS	0.004	0.01	$0.187 \pm 0.007$	$2292 \pm 40$
wa014bs21	4.5	linear	BLISS	0.028	0.023	$0.224 \pm 0.018$	$2292 \pm 97$
wa014bs41	8.0	linear	-	-	-	$0.182 \pm 0.022$	$1637 \pm 120$

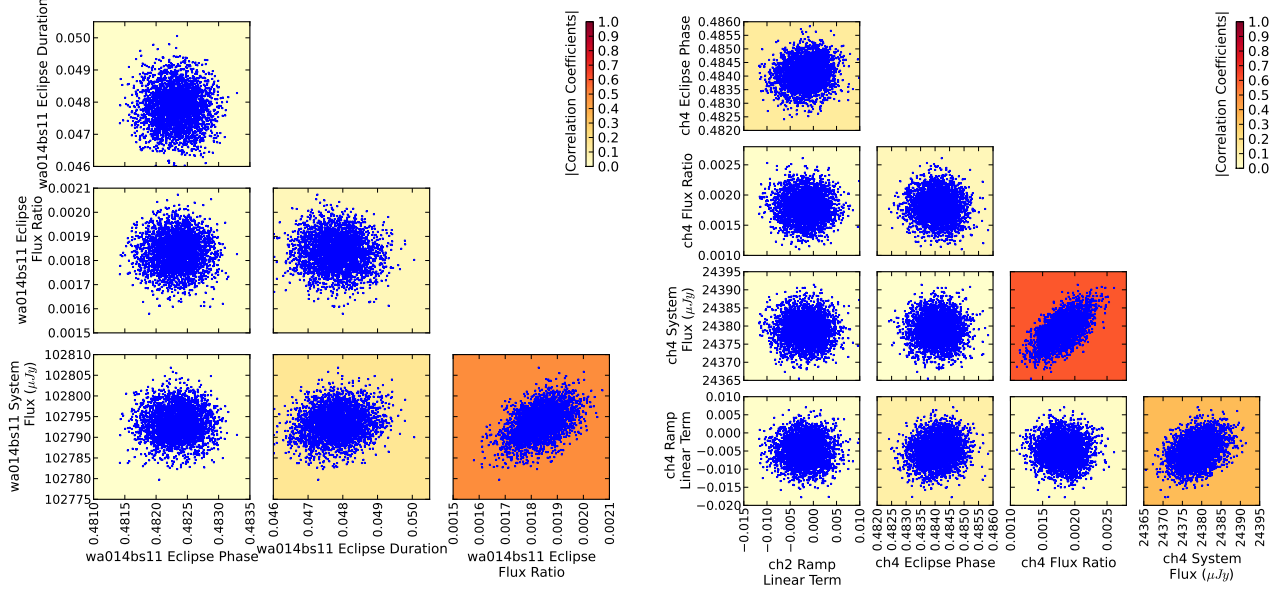


FIG. 13.— **Left:** Parameter correlations for wa014bs11. The background color depicts the absolute value of the correlation coefficient. **Right:** Parameter correlations for wa014bs21 and wa014bs41, produced in the joint fit. The background color depicts the absolute value of the correlation coefficient. Every  $100^{\text{th}}$  step in the MCMC chain is used, to decorrelate consecutive values in both datasets.

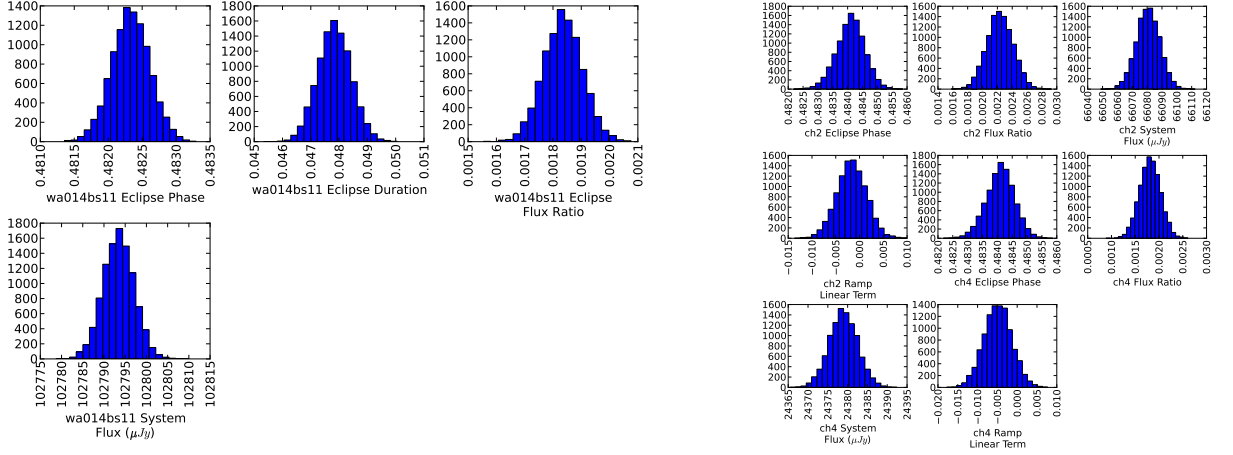


FIG. 14.— **Left:** Parameter histograms for wa014bs11. **Right:** Parameter histograms for wa014bs21 and wa014bs41, produced in the joint fit. Every  $100^{\text{th}}$  step in the MCMC chain is used, to decorrelate consecutive values in both data sets.

nication, 2010). The convergence was tested every  $10^5$  steps. Our models converged after 5%, and the Gelman & Rubin (1992) diagnostic dropped below 1% for all free parameters. Figure 13 and Figure 14 show marginal posterior distributions (the parameter histograms) and plots of the pairwise correlations for channel 1 and joint channels 2 and 4. These confirm that the phase space minimum is global, and define the value of parameter uncertainties. The best-fit eclipse light curve parameters from the joint fit and the best model fits are given in

Table 6 and Table 7 respectively.

## 6. ORBIT

We fit the midpoint times from the Spitzer lightcurves simultaneously with the available radial velocity curves and transit photometry, in order to provide updated measurements of system orbital parameters (see Table 8). The timing of secondary eclipse is a strong constraint on the shape and orientation of the orbit. The two eclipses occur at phases  $0.4825 \pm 0.0003$  and  $0.4841 \pm 0.0005$  (using the Joshi et al. 2009

ephemeris), with a weighted mean after a 37 s light-time correction of  $0.48273 \pm 0.00025$ , indicating that  $e \cos \omega = -0.02713 \pm 0.00039$ . The phases differ from each other by approximately  $3\sigma$ , but depend strongly on the accuracy of the ephemeris used to compute them.

TABLE 8  
ECCENTRIC ORBITAL MODEL.

Parameter	Value
$e \sin \omega^a$	$0.0831 \pm 0.0021$
$e \cos \omega^a$	$-0.02557 \pm 0.00038$
$e$	$0.087 \pm 0.002$
$\omega$ ( $^\circ$ )	$-107.1 \pm 0.5$
$P$ (days) <sup>a</sup>	$2.2437661 \pm 0.0000011$
$T_0$ (MJD) <sup>a</sup>	$2454827.06666 \pm 0.00024$
$K$ (ms <sup>-1</sup> ) <sup>a</sup>	$990 \pm 3$
$\gamma$ (ms <sup>-1</sup> ) <sup>a</sup>	$-4,987.9 \pm 1.6$
$\chi^2$	162

<sup>a</sup>Free parameter in MCMC fit

We fit a Keplerian orbit model to our secondary eclipse times along with radial velocity data from Husnoo et al. (2011) and Joshi et al. (2009), and transit timing data from both amateur observers and WASP-14b's discovery paper (Joshi et al. 2009). The entire data set comprised 38 RV points, six of which were removed due to the Rossiter-McLaughlin effect, 30 transits, and two eclipses (see Table 9). All times were adjusted to BJD<sub>TDB</sub> (Eastman et al. 2010), and 37 seconds were subtracted from the eclipse times to approximately account for the eclipse-transit light-time. The errors were estimated using our MCMC routine. From this fit we determine that  $e = 0.087 \pm 0.002$  and  $\omega = 107.1 \pm 0.5^\circ$ . With our new data, we refine the ephemeris to  $T_{BJDTDB} = 2454827.06666(24) + 2.2437661(11)N$ , where  $T$  is the time of transit and  $N$  is the number of orbits elapsed since the transit time (see Table 8). We find that the new ephemeris dampens the difference between the two eclipse phases to less than  $1.6\sigma$ . Performing an ephemeris fit to the transit and eclipse data separately shows that the transit and eclipse periods differ by  $(1.1 \pm 0.8) \times 10^{-5}$  days, a  $1.5\sigma$  result that limits apsidal motion,  $\dot{\omega}$ , to less than  $0.0024^\circ \text{day}^{-1}$  at the  $3\sigma$  level (Giménez & Bastero 1995).

The results confirm an eccentric orbit for WASP-14b and improve knowledge of other orbital parameters.

## 7. ATMOSPHERE

We modeled the dayside atmosphere of WASP-14b using the exoplanetary atmospheric modeling method developed by Madhusudhan & Seager (2009, 2010). We use a 1D line-by-line radiative transfer code to model the planetary atmosphere under the assumption of local thermodynamic equilibrium (LTE), hydrostatic equilibrium, and global energy balance at the top of the atmosphere. The latter condition assumes that the integrated emergent planetary flux balances the integrated incident stellar flux, accounting for the Bond albedo ( $A_B$ ) and possible redistribution of energy onto the night side. Our model uses parametrized prescriptions to retrieve the temperature structure and chemical composition from the observations, as opposed to assuming radiative and chemical equilibrium with fixed elemental abundances (Burrows et al. 2008; Fortney et al. 2008).

We explore the model parameter space in search of the best-fitting models for a given data set. The model parameterization is described by Madhusudhan & Seager (2009,

TABLE 9  
TRANSIT TIMING DATA.

Mid-Transit Time (BJD <sub>TDB</sub> )	Uncertainty	Source <sup>a</sup>
2455695.4082	0.0012	V. Slesarenko, E. Sokov <sup>d</sup>
2455668.4790	0.0011	František Lomoz
2455652.7744	0.0014	Stan Shadick, C. Shiels <sup>b</sup>
2455650.5307	0.0018	Lubos Brát
2455650.52789	0.00076	Martin Vrašťák
2455650.52566	0.00067	Jaroslav Trnka
2455632.5807	0.0011	E. Sokov, K. N. Naumov <sup>d</sup>
2455318.45101	0.00085	Anthony Ayiomamitis
2455302.7464	0.0010	Stan Shadick <sup>b</sup>
2455264.6021	0.0012	Hana Kučáková
2455264.6017	0.0013	Radek Kocián <sup>c</sup>
2455219.7290	0.0012	Lubos Brát
2454979.643	0.003	Wiggins, AXA
2454968.426	0.001	Srdoc, AXA
2454950.4831	0.0021	Jesionkiewicz, AXA
2454950.4746	0.0014	Lubos Brát
2454950.4745	0.0018	Hana Kučáková
2454950.4731	0.0021	Pavel Marek
2454950.4728	0.0014	Wardak, AXA
2454943.7427	0.0006	Dvorak, AXA
2454941.49799	0.00081	Jaroslav Trnka
2454941.4916	0.0019	František Lomoz
2454934.765	0.001	Brucy Gary, AXA
2454932.5246	0.0014	Radek Dřevěný
2454932.5232	0.0011	Lubos Brát
2454932.5222	0.0013	Jaroslav Trnka
2454932.5219	0.0015	T. Hynek, K. Onderková
2454914.5753	0.0008	Naves, AXA
2454887.6457	0.0014	Georgio, AXA

<sup>a</sup>The Amateur Exoplanet Archive (AXA), <http://brucegary.net/AXA/x.htm> and Transiting ExoplanetS and Candidates group (TRESA), <http://var2.astro.cz/EN/tresca/index.php> supply their data to the Exoplanet Transit Database (ETD), <http://var2.astro.cz/ETD/> which performs the uniform transit analysis described by Poddaný et al. (2010). The ETD web site provided the AXA and TRESA numbers in this table, which were converted to BJD<sub>TDB</sub>.

<sup>b</sup>Physics and Engineering Physics Department, University of Saskatchewan, Saskatoon, Saskatchewan, Canada, S7N 5E2

<sup>c</sup>Kocián R., Johann Palisa, Observatory and Planetarium, Technical University Ostrava, 17. listopadu 15, CZ-708 33 Ostrava, Czech Republic

<sup>d</sup>Sokov E., Naumov K., Slesarenko V. et al., Pulkovo Observatory of RAS, Saint-Petersburg, Russia

<sup>e</sup>Municipal Observatory in Slany Czech Republic

<sup>f</sup>Project Eridanus, Observatory and Planetarium of Johann Palisa in Ostrava

2010). The sources of opacity in the model include molecular absorption due to H<sub>2</sub>O, CO, CH<sub>4</sub>, CO<sub>2</sub>, TiO, and VO, and collision-induced absorption (CIA) due to H<sub>2</sub>-H<sub>2</sub>. Our molecular line lists are obtained from Freedman et al. (2008), Freedman (personal communication, 2009), Rothman et al. (2005); Karkoschka & Tomasko (2010), and Karkoschka (personal communication, 2011). Our CIA opacities are obtained from Borysow et al. (1997) and Borysow (2002). We explore the model parameter space using a MCMC scheme, as described by Madhusudhan & Seager (2010). However, since the number of model parameters ( $N = 10$ ) exceed the number of data points ( $N_{\text{data}} = 3$ ), our goal is not to find a unique fit to the data but, primarily, to rule out regions of model phase space that are excluded by the data. In order to compute the model planet-star flux ratios to match with the data, we divide the planetary spectrum by a Kurucz model of the stellar spectrum derived from Castelli & Kurucz (2004). Our models allow constraints on the temperature structure, molecular mixing ratios, and a joint constraint on the albedo and day-

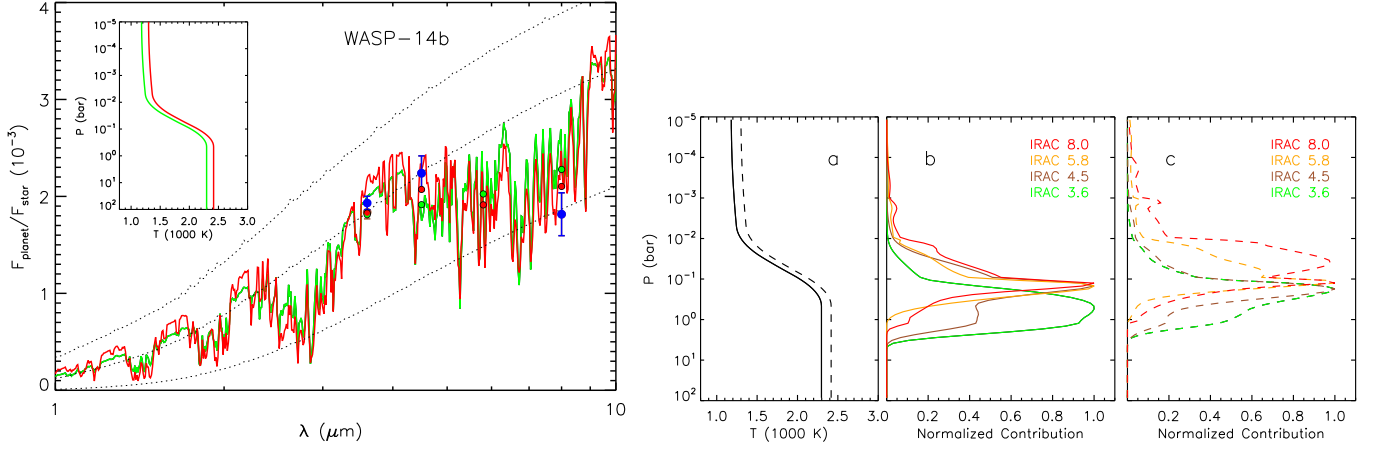


FIG. 15.— **Left:** Observations and model spectra for dayside emission from WASP-14b. The blue filled circles with error bars show our observations in Spitzer channel 1 (3.6  $\mu\text{m}$ ), 2 (4.5  $\mu\text{m}$ ), and 4 (8.0  $\mu\text{m}$ ). For the 3.6  $\mu\text{m}$  channel, two values are shown, in blue and brown, corresponding to different ramp models used in deriving the eclipse depths (see Section 5.1). The green and red curves in the main panel show two model spectra without thermal inversions and with different chemical composition; the corresponding pressure-temperature ( $P$ - $T$ ) profiles are shown in the inset. The green and red circles show the model spectra integrated in the Spitzer IRAC bandpasses. Both profiles lead to good fit to the observations, but with different molecular compositions. The green model has molecular abundances in chemical equilibrium assuming solar elemental abundances. The red model has 10 times lower CO and 6 times higher  $\text{H}_2\text{O}$  compared to solar abundance chemistry, and provides a better fit to the data compared to the green model. The black dotted lines show three blackbody planet spectra at 1500 K, 2200 K, and 2600 K. **Right:**  $P$ - $T$  profiles and contribution functions corresponding to the models shown on the left panel. Panel *a* shows two  $P$ - $T$  profiles that correspond to the  $P$ - $T$  profiles in the inset figure, left panel. Solid line corresponds to the green line, and dotted line to the red line. Panel *b* and *c* show the contribution functions in the four *Spitzer* channels for each model. The legend shows the channel center wavelength in  $\mu\text{m}$  and the curves are color-coded by the channel. All the contribution functions are normalized to unity.

night redistribution.

We find that strong constraints can be placed on the presence of a thermal inversion in WASP-14b even with our current small set of observations. At an irradiation of  $3 \times 10^9 \text{ ergs}^{-1}\text{cm}^{-2}$ , WASP-14b falls in the class of extremely irradiated planets that are predicted to host thermal inversions according to the TiO/VO hypothesis of Fortney et al. (2008). However, the present observations do not show any distinct evidence of a thermal inversion in the dayside atmosphere of WASP-14b. While the brightness temperatures in the 3.6 and 4.5  $\mu\text{m}$  channels are consistent with a blackbody spectrum of the planet at  $T \sim 2200 \text{ K}$ , the 8 micron flux deviates substantially from the assumption of a blackbody with a brightness temperature of  $1637 \pm 120 \text{ K}$ . In the presence of a thermal inversion, the flux in the 8  $\mu\text{m}$  channel is expected to be much higher than the fluxes in the 3.6 and 4.5  $\mu\text{m}$  channels due to emission features of water vapor, and methane, if present. The low flux observed at 8  $\mu\text{m}$ , therefore, implies strong water vapor and/or methane in absorption, implying the lack of a significant temperature inversion (see Madhusudhan & Seager 2010 for a discussion on inferring thermal inversions). We also note that, as mentioned in Section 5.1, the observations yield different planet-star flux contrasts in the 3.6  $\mu\text{m}$  channel for different choices of ramp models. However, as shown in Figure 15, the two extreme values are still consistent at the 1- $\sigma$  level, and as such, lead to similar model conclusions.

The observations provide only marginal constraints on the chemistry, although there are hints of enhanced  $\text{H}_2\text{O}$  over CO. We find that the observations can all be explained by compositions within a factor of 10 of those obtained from thermochemical equilibrium assuming solar abundances ( $\text{TE}_{\text{solar}}$ ). Figure 15, shows two model spectra along with the observations, one with molecular abundances at  $\text{TE}_{\text{solar}}$ , and another with 10 times lower CO and 6 times higher  $\text{H}_2\text{O}$ . The latter model fits the data marginally better. A slightly lower CO is favored because of the slightly higher 4.5  $\mu\text{m}$  flux compared to the 3.6  $\mu\text{m}$  flux, which means lower absorption due to CO. Higher absorption due to  $\text{H}_2\text{O}$  is favored by the low 8

$\mu\text{m}$  point. In principle, a lower CO and a higher  $\text{H}_2\text{O}$ , compared to  $\text{TE}_{\text{solar}}$  values are both possible by having a lower C/O ratio compared to the solar C/O ratio (0.54). However, more data would be required to confirm the low CO requirement, because a blackbody of  $\sim 2200 \text{ K}$  fits the 3.6 and 4.5  $\mu\text{m}$  points just as well. We have also considered models with high C/O ratios (e.g.  $\text{C/O} \geq 1$ ), which can lead to strong  $\text{CH}_4$  absorption in the 3.6  $\mu\text{m}$  and 8  $\mu\text{m}$  channels (e.g., Madhusudhan et al. 2011a,b), instead of  $\text{H}_2\text{O}$  absorption in the low C/O models shown in Figure 15. However, we find that the amount of methane possible in high C/O models of WASP-14b is inadequate to cause the strong absorption in the 3.6  $\mu\text{m}$  and 8  $\mu\text{m}$  channels required by the data; note that in high C/O models  $\text{H}_2\text{O}$  is depleted and  $\text{CH}_4$  is enhanced. This would be a good motivation for future observations in the near IR, from ground and space, to place further constraints on the temperature structure and composition, especially the C/O ratio, of the dayside atmosphere of WASP-14b.

The models explaining the observations require relatively low day-night energy redistribution in WASP-14b. The large brightness temperature in the 3.6  $\mu\text{m}$  channel, which probes the deep atmosphere at pressures of  $\sim 1 \text{ bar}$ , is indicative of a hot planet photosphere. For zero-albedo, we find that about  $\sim 0.25$  of the energy incident on the dayside can be redistributed to the night side. For non-zero albedos this fraction is even lower; since the quantity we constrain is  $\eta = (1-A_B)(1-f_r)$ , where  $A_B$  is the Bond albedo, and  $f_r$  is the fraction of the dayside incident energy redistributed to the night-side. Our finding of low redistribution can be verified by thermal light curves in the future (e.g., Knutson et al. 2007, 2009a).

## 8. DISCUSSION

The absence of a thermal inversion in the dayside atmosphere of WASP-14b provides important constraints on inversion-causing phenomena in irradiated atmospheres. The canonical argument for thermal inversions in hot Jupiter atmospheres is via TiO and VO. Hubeny et al. (2003) and Fortney et al. (2008) suggested the possibility that TiO and VO

could exist in gas phase in high-temperature atmospheres - the TiO/VO hypothesis. Being strong absorbers of incident visible light, TiO and VO could cause thermal inversions in hot Jupiter atmospheres. On the other hand, Spiegel *et al.* (2009) showed that the high mean molecular masses of TiO and VO would lead to significant gravitational settling of these molecules, thereby depleting them from the upper atmospheres, unless strong vertical mixing keeps them aloft. Additionally, the abundances of inversion-causing molecules might also be influenced by stellar activity and photochemistry (Knutson *et al.* 2010). Consequently, the real cause of thermal inversions in irradiated atmospheres is currently unknown. Nevertheless, models used to infer thermal inversions in the literature have either used parametrized visible opacity sources (Burrows *et al.* 2008) or parametric temperature profiles (Madhusudhan & Seager 2009, also used in the present work). To first order, the lack of a thermal inversion in WASP-14b might indicate that the vertical mixing in the dayside atmosphere of WASP-14b is weaker compared to the downward diffusion of TiO and VO.

Until now, *Spitzer* observations have provided us with a range of hot Jupiter planets that are strongly irradiated by their parent stars, with brightness temperatures between 1000-2000 K. The inferences of thermal inversions from thermal spectra of hot Jupiters result from observing flux excesses in molecular bands where strong absorption is expected (Madhusudhan & Seager 2010). In principle, detection of a thermal inversion in high S/N observations is possible with just two *Warm Spitzer* channels if there is a high difference in fluxes in channels 1 and 2. Similar conclusions have been reached based on the flux excesses in certain *Spitzer* channels by e.g., Knutson *et al.* (2008, 2009a); Madhusudhan & Seager (2010); Machalek *et al.* (2009); O'Donovan *et al.* (2010) and Christiansen *et al.* (2010). Based on the TiO/VO hypothesis described above, Fortney *et al.* (2008) suggested that depending on the level of irradiation from their parent star, irradiated planets can fall into two categories: the very highly irradiated atmospheres that host thermal inversions and the less irradiated ones that do not. However, recent observations have revealed several counter-examples to this hypothesis. Machalek *et al.* (2008, 2009) present evidence for a temperature inversion in XO-1b, despite low irradiation of the planet ( $T_{eq} = 1209$  K), while Fressin *et al.* (2010) show no thermal inversion, although TrES-3b is a highly irradiated planet ( $T_{eq} = 1643$  K). Similarly, WASP-12b, one of the most irradiated hot Jupiters known, has also been reported to lack a significant thermal inversion (Madhusudhan *et al.* 2011a). In this paper, we present WASP-14b as another example that demonstrates that planets studied to date cover a wide range and do not fall distinctively into two categories (Gillon *et al.* 2010). It is possible, that additional parameters (e.g., metallicity or surface gravity) influence the presence or the absence of a temperature inversion. However, more observations are needed to explain the lack of the inversion in this planet.

## 9. CONCLUSIONS

During two secondary eclipse events, *Spitzer* observed WASP-14b in the three IRAC channels: 3.6, 4.5, and 8.0  $\mu\text{m}$ . All eclipses have a high S/N ratio (3.6  $\mu\text{m}$  channel  $\sim 25$ , 4.5  $\mu\text{m}$  channel  $\sim 12$ , 8.0  $\mu\text{m}$  channel  $\sim 8$ ), which allowed us to constrain the planetary spectrum and orbital parameters.

Our observations in the three IRAC channels probe the atmosphere at pressures between 0.01 and 1 bar and indicate the

absence of a significant thermal inversion in the dayside atmosphere of WASP-14b. The lack of a thermal inversion in the highly irradiated atmosphere of WASP-14b contradicts previous predictions that the most irradiated hot Jupiters should have thermal inversions due to gaseous TiO/VO (Fortney *et al.* 2008). Additionally, our observations place nominal constraints on the chemical composition and day-night energy redistribution in the atmosphere of WASP-14b. We find that the data can be explained by non-inversion models in chemical equilibrium with nearly solar abundances. A factor of 10 less CO and a factor of 6 higher H<sub>2</sub>O, compared to those obtained with solar abundances, explain the data to within the  $1\sigma$  uncertainties, on average. Such CO depletion and H<sub>2</sub>O enhancement are, in principle, possible in chemical equilibrium with C/O ratios lower than solar. More data are required to better constrain the atmospheric composition of WASP-14b.

Because the planet is much brighter than its predicted equilibrium temperature for uniform redistribution ( $T_{eq} = 1866\text{K}$ ), the best-fitting models require relatively low day-night energy redistribution in WASP-14b. We find an upper limit on the fraction of energy redistributed to the night side to be 0.25 (for zero Bond albedo).

WASP-14b is one of the most massive transiting planets known along with CoRoT-3b (Triaud *et al.* 2009; Deleuil *et al.* 2008), HAT-P-2b (Bakos *et al.* 2007; Winn *et al.* 2007; Loeillet *et al.* 2008b), XO-3b (Hébrard *et al.* 2008; Johns-Krull *et al.* 2008; Winn *et al.* 2008), and WASP-18b (Nymeyer *et al.* 2011). With the exception of WASP-18b, all of these objects have large eccentric orbits. Classic theories suggest that there is a trend for the inner planets to have circular orbits due to tidal orbital decay. At distances  $a < 0.1$  AU any orbital eccentricity should induce strong tidal energy dissipation, leading to circular orbits in relatively short time scales (typically a few Myr, compared to common system ages of few Gyr). However, Pont *et al.* (2011) argue that the circularization timescale scales with the planet-star mass ratio, and is also a steep function of the orbital separation, scaled to the planet radius (see their Figure 3). For planets with  $M > M_J$ , the mass-period relation (see their Figure 2) suggests that heavier planets get circularized very close to their parent star, or they do not ever reach circularization in their lifetime. A possible explanation is that the planet raises tides on its host star strong enough that the angular momentum of the planet is transferred to the stellar spin, and the planet gets swallowed by the star. This does not oppose the classical tide theory (e.g., Goldreich & Soter 1966), rather suggests that stopping mechanisms and tidal circularization are related. WASP-14b also has unusually high density for hot Jupiters, similar to that of some rocky planets ( $4.6 \text{ g cm}^{-3}$ ). Having a strong signal makes this planet ideal for further exploration of this topic and of possible formation mechanisms of similar objects.

We thank Heather Knutson for providing the data at 3.6  $\mu\text{m}$  *Spitzer* observation prior to their public release.

We also thank contributors to SciPy, Matplotlib, and the Python Programming Language, W. Landsman and other contributors to the Interactive Data Language Astronomy Library, the free and open-source community, the NASA Astrophysics Data System, and the JPL Solar System Dynamics group for free software and services. This work is based on observations made with the *Spitzer* Space Telescope, which is operated by the Jet Propulsion Laboratory, California Institute of Technology under a contract with NASA. Support for this work was provided by NASA through an award issued by JPL/Caltech.

## REFERENCES

- Anderson, D. R., Hellier, C., Gillon, M., Triaud, A. H. M. J., Smalley, B., Hebb, L., Collier Cameron, A., Maxted, P. F. L., Queloz, D., West, R. G., Bentley, S. J., Enoch, B., Horne, K., Lister, T. A., Mayor, M., Parley, N. R., Pepe, F., Pollacco, D., Ségransan, D., Udry, S., & Wilson, D. M. 2010, *ApJ*, 709, 159
- Bakos, G. Á., Kovács, G., Torres, G., Fischer, D. A., Latham, D. W., Noyes, R. W., Sasselov, D. D., Mazeh, T., Shporer, A., Butler, R. P., Stefanik, R. P., Fernández, J. M., Sozzetti, A., Pál, A., Johnson, J., Marcy, G. W., Winn, J. N., Sipőcz, B., Lázár, J., Papp, I., & Sári, P. 2007, *ApJ*, 670, 826
- Balachandran, S. 1995, *ApJ*, 446, 203
- Ballard, S., Charbonneau, D., Deming, D., Knutson, H. A., Christiansen, J. L., Holman, M. J., Fabrycky, D., Seager, S., & A'Hearn, M. F. 2010, *PASP*, 122, 1341
- Boesgaard, A. M. & Tripicco, M. J. 1986, *ApJ*, 303, 724
- Borysow, A. 2002, *A&A*, 390, 779
- Borysow, A., Jorgensen, U. G., & Zheng, C. 1997, *A&A*, 324, 185
- Burrows, A., Budaj, J., & Hubeny, I. 2008, *ApJ*, 678, 1436
- Campo, C. J., Harrington, J., Hardy, R. A., Stevenson, K. B., Nymeyer, S., Ragozzine, D., Lust, N. B., Anderson, D. R., Collier-Cameron, A., Blecic, J., Britt, C. B. T., Bowman, W. C., Wheatley, P. J., Lored, T. J., Deming, D., Hebb, L., Hellier, C., Maxted, P. F. L., Pollacco, D., & West, R. G. 2011, *ApJ*, 727, 125
- Castelli, F. & Kurucz, R. L. 2004, *ArXiv Astrophysics e-prints*
- Charbonneau, D., Allen, L. E., Megeath, S. T., Torres, G., Alonso, R., Brown, T. M., Gilliland, R. L., Latham, D. W., Mandushev, G., O'Donovan, F. T., & Sozzetti, A. 2005, *ApJ*, 626, 523
- Christiansen, J. L., Ballard, S., Charbonneau, D., Madhusudhan, N., Seager, S., Holman, M. J., Wellnitz, D. D., Deming, D., A'Hearn, M. F., & the EPOXI Team. 2010, *ApJ*, 710, 97
- Collier Cameron, A., Pollacco, D., Street, R. A., Lister, T. A., West, R. G., Wilson, D. M., Pont, F., Christian, D. J., Clarkson, W. I., Enoch, B., Evans, A., Fitzsimmons, A., Haswell, C. A., Hellier, C., Hodgkin, S. T., Horne, K., Irwin, J., Kane, S. R., Keenan, F. P., Norton, A. J., Parley, N. R., Osborne, J., Ryans, R., Skillen, I., & Wheatley, P. J. 2006, *MNRAS*, 373, 799
- Collier Cameron, A., Wilson, D. M., West, R. G., Hebb, L., Wang, X.-B., Aigrain, S., Bouchy, F., Christian, D. J., Clarkson, W. I., Enoch, B., Esposito, M., Guenther, E., Haswell, C. A., Hébrard, G., Hellier, C., Horne, K., Irwin, J., Kane, S. R., Loeillet, B., Lister, T. A., Maxted, P., Mayor, M., Moutou, C., Parley, N., Pollacco, D., Pont, F., Queloz, D., Ryans, R., Skillen, I., Street, R. A., Udry, S., & Wheatley, P. J. 2007, *MNRAS*, 380, 1230
- Deleuil, M., Deeg, H. J., Alonso, R., Bouchy, F., Rouan, D., Auvergne, M., Baglin, A., Aigrain, S., Almenara, J. M., Barbieri, M., Barge, P., Bruntt, H., Bordé, P., Collier Cameron, A., Csizmadia, S., de La Reza, R., Dvorak, R., Erikson, A., Fridlund, M., Gandolfi, D., Gillon, M., Guenther, E., Guillot, T., Hatzes, A., Hébrard, G., Jorda, L., Lammer, H., Léger, A., Liebaria, A., Loeillet, B., Mayor, M., Mazeh, T., Moutou, C., Ollivier, M., Pätzold, M., Pont, F., Queloz, D., Rauer, H., Schneider, J., Shporer, A., Wuchterl, G., & Zucker, S. 2008, *A&A*, 491, 889
- Désert, J.-M., Lecavelier des Etangs, A., Hébrard, G., Sing, D. K., Ehrenreich, D., Ferlet, R., & Vidal-Madjar, A. 2009, *ApJ*, 699, 478
- Eastman, J., Siverd, R., & Gaudi, B. S. 2010, *PASP*, 122, 935
- Fazio, G. G. et al. 2004, *Astrophys. J. Suppl. Ser.*, 154, 10
- Fortney, J. J., Ladders, K., Marley, M. S., & Freedman, R. S. 2008, *ApJ*, 678, 1419
- Fortney, J. J., Marley, M. S., & Barnes, J. W. 2007, *ApJ*, 659, 1661
- Freedman, R. S., Marley, M. S., & Ladders, K. 2008, *ApJS*, 174, 504
- Fressin, F., Knutson, H. A., Charbonneau, D., O'Donovan, F. T., Burrows, A., Deming, D., Mandushev, G., & Spiegel, D. 2010, *ApJ*, 711, 374
- Gelman, A. 2002, *Encyclopedia of Environmetrics*, 3, 1634
- Gelman, A. & Rubin, D. 1992, *Statistical Science*, 7, 457
- Gillon, M., Lanotte, A. A., Barman, T., Miller, N., Demory, B.-O., Deleuil, M., Montalbán, J., Bouchy, F., Collier Cameron, A., Deeg, H. J., Fortney, J. J., Fridlund, M., Harrington, J., Magain, P., Moutou, C., Queloz, D., Rauer, H., Rouan, D., & Schneider, J. 2010, *A&A*, 511, A3+
- Giménez, A. & Bastero, M. 1995, *Ap&SS*, 226, 99
- Goldreich, P. & Soter, S. 1966, *Icarus*, 5, 375
- Harrington, J., Luszcz, S., Seager, S., Deming, D., & Richardson, L. J. 2007, *Nature*, 447, 691
- Hébrard, G., Bouchy, F., Pont, F., Loeillet, B., Rabus, M., Bonfils, X., Moutou, C., Boisse, I., Delfosse, X., Desort, M., Eggenberger, A., Ehrenreich, D., Forveille, T., Lagrange, A.-M., Lovis, C., Mayor, M., Pepe, F., Perrier, C., Queloz, D., Santos, N. C., Ségransan, D., Udry, S., & Vidal-Madjar, A. 2008, *A&A*, 488, 763
- Hubeny, I., Burrows, A., & Sudarsky, D. 2003, *ApJ*, 594, 1011
- Husnoo, N., Pont, F., Hébrard, G., Simpson, E., Mazeh, T., Bouchy, F., Moutou, C., Arnold, L., Boisse, I., Díaz, R. F., Eggenberger, A., & Shporer, A. 2011, *MNRAS*, 413, 2500
- Johns-Krull, C. M., McCullough, P. R., Burke, C. J., Valenti, J. A., Janes, K. A., Heasley, J. N., Prato, L., Bissinger, R., Fleenor, M., Foote, C. N., Garcia-Melendo, E., Gary, B. L., Howell, P. J., Mallia, F., Masi, G., & Vanmunster, T. 2008, *ApJ*, 677, 657
- Joshi, Y. C., Pollacco, D., Collier Cameron, A., Skillen, I., Simpson, E., Steele, I., Street, R. A., Stempels, H. C., Christian, D. J., Hebb, L., Bouchy, F., Gibson, N. P., Hébrard, G., Keenan, F. P., Loeillet, B., Meaburn, J., Moutou, C., Smalley, B., Todd, I., West, R. G., Anderson, D. R., Bentley, S., Enoch, B., Haswell, C. A., Hellier, C., Horne, K., Irwin, J., Lister, T. A., McDonald, I., Maxted, P., Mayor, M., Norton, A. J., Parley, N., Perrier, C., Pont, F., Queloz, D., Ryans, R., Smith, A. M. S., Udry, S., Wheatley, P. J., & Wilson, D. M. 2009, *MNRAS*, 392, 1532
- Karkoschka, E. & Tomasko, M. G. 2010, *Icarus*, 205, 674
- Knutson, H. A., Charbonneau, D., Allen, L. E., Burrows, A., & Megeath, S. T. 2008, *ApJ*, 673, 526
- Knutson, H. A., Charbonneau, D., Burrows, A., O'Donovan, F. T., & Mandushev, G. 2009a, *ApJ*, 691, 866
- Knutson, H. A., Charbonneau, D., Cowan, N. B., Fortney, J. J., Showman, A. P., Agol, E., & Henry, G. W. 2009b, *ApJ*, 703, 769
- Knutson, H. A., Charbonneau, D., Deming, D., & Richardson, L. J. 2007, *PASP*, 119, 616
- Knutson, H. A., Howard, A. W., & Isaacson, H. 2010, *ApJ*, 720, 1569
- Knutson, H. A., Madhusudhan, N., Cowan, N. B., Christiansen, J. L., Agol, E., Deming, D., Désert, J.-M., Charbonneau, D., Henry, G. W., Homeier, D., Langton, J., Laughlin, G., & Seager, S. 2011, *ApJ*, 735, 27
- Liddle, A. R. 2007, *MNRAS*, 377, L74
- Loeillet, B., Bouchy, F., Deleuil, M., Royer, F., Bouret, J. C., Moutou, C., Barge, P., de Laverny, P., Pont, F., Recio-Blanco, A., & Santos, N. C. 2008a, *A&A*, 479, 865
- Loeillet, B., Shporer, A., Bouchy, F., Pont, F., Mazeh, T., Beuzit, J. L., Boisse, I., Bonfils, X., da Silva, R., Delfosse, X., Desort, M., Ecuivillon, A., Forveille, T., Galland, F., Gallenne, A., Hébrard, G., Lagrange, A.-M., Lovis, C., Mayor, M., Moutou, C., Pepe, F., Perrier, C., Queloz, D., Ségransan, D., Sivan, J. P., Santos, N. C., Tsodikovich, Y., Udry, S., & Vidal-Madjar, A. 2008b, *A&A*, 481, 529
- Lust, N. B., Britt, D. T., Harrington, J., Nymeyer, S., Stevenson, K. B., Lust, E. L., Bowman, W. C., & Fraine, J. 2012, *ApJ*, submitted
- Machalek, P., McCullough, P. R., Burke, C. J., Valenti, J. A., Burrows, A., & Hora, J. L. 2008, *ApJ*, 684, 1427
- Machalek, P., McCullough, P. R., Burrows, A., Burke, C. J., Hora, J. L., & Johns-Krull, C. M. 2009, *ApJ*, 701, 514
- Madhusudhan, N., Harrington, J., Stevenson, K. B., Nymeyer, S., Campo, C. J., Wheatley, P. J., Deming, D., Blecic, J., Hardy, R. A., Lust, N. B., Anderson, D. R., Collier-Cameron, A., Britt, C. B. T., Bowman, W. C., Hebb, L., Hellier, C., Maxted, P. F. L., Pollacco, D., & West, R. G. 2011a, *Nature*, 469, 64
- Madhusudhan, N., Mousis, O., Johnson, T. V., & Lunine, J. I. 2011b, *ArXiv e-prints*
- Madhusudhan, N. & Seager, S. 2009, *ApJ*, 707, 24
- , 2010, *ApJ*, 725, 261
- Mandel, K. & Agol, E. 2002, *ApJ*, 580, L171
- Morales-Calderón, M., Stauffer, J. R., Kirkpatrick, J. D., Carey, S., Gelino, C. R., Barrado y Navascués, D., Rebull, L., Lowrance, P., Marley, M. S., Charbonneau, D., Patten, B. M., Megeath, S. T., & Buzasi, D. 2006, *ApJ*, 653, 1454
- Nymeyer, S., Harrington, J., Hardy, R. A., Stevenson, K. B., Campo, C. J., Madhusudhan, N., Collier-Cameron, A., Blecic, J., Bowman, W. C., Britt, C. B. T., Cubillos, P., Hellier, C., Gillon, M., Maxted, P. F. L., Hebb, L., Wheatley, P. J., Pollacco, D., & Anderson, D. 2011, *ApJ*, submitted
- O'Donovan, F. T., Charbonneau, D., Harrington, J., Madhusudhan, N., Seager, S., Deming, D., & Knutson, H. A. 2010, *ApJ*, 710, 1551
- Poddany, S., Brát, L., & Pejcha, O. 2010, *ArXiv Astrophysics e-prints*, 15, 297
- Pollacco, D., Skillen, I., Collier Cameron, A., Christian, D., Irwin, J., Lister, T., Street, R., West, R., Clarkson, W., Evans, N., Fitzsimmons, A., Haswell, C., Hellier, C., Hodgkin, S., Horne, K., Jones, B., Kane, S., Keenan, F., Norton, A., Osborne, J., Ryans, R., & Wheatley, P. 2006, *Ap&SS*, 304, 253
- Pont, F., Husnoo, N., Mazeh, T., & Fabrycky, D. 2011, *MNRAS*, 414, 1278
- Pont, F., Zucker, S., & Queloz, D. 2006, *MNRAS*, 373, 231
- Reach, W. T., Megeath, S. T., Cohen, M., Hora, J., Carey, S., Surace, J., Willner, S. P., Barmby, P., Wilson, G., Glaccum, W., Lowrance, P., Marengo, M., & Fazio, G. G. 2005, *PASP*, 117, 978
- Rothman, L. S., Jacquemart, D., Barbe, A., Chris Benner, D., Birk, M., Brown, L. R., Carleer, M. R., Chackerian, C., Chance, K., Coudert, L. H., Dana, V., Devi, V. M., Flaud, J.-M., Gamache, R. R., Goldman, A., Hartmann, J.-M., Jucks, K. W., Maki, A. G., Mandin, J.-Y., Massie, S. T., Orphal, J., Perrin, A., Rinsland, C. P., Smith, M. A. H., Tennyson, J., Tolchenov, R. N., Toth, R. A., Vander Auwera, J., Varanasi, P., & Wagner, G. 2005, *J. Quant. Spec. Radiat. Transf.*, 96, 139
- Seager, S. & Deming, D. 2009, *ApJ*, 703, 1884
- , 2010, *ARA&A*, 48, 631
- Spiegel, D. S., Silverio, K., & Burrows, A. 2009, *ApJ*, 699, 1487
- Stevenson, K. B., Harrington, J., Fortney, J., Lored, T. J., Hardy, R. A., Nymeyer, S., Bowman, W. C., Cubillos, P., Bowman, M. O., & Hardin, M. 2011, *ArXiv e-prints*

- Stevenson, K. B., Harrington, J., Nymeyer, S., Madhusudhan, N., Seager, S., Bowman, W. C., Hardy, R. A., Deming, D., Rauscher, E., & Lust, N. B. 2010, *Nature*, 464, 1161
- Tinetti, G., Vidal-Madjar, A., Liang, M.-C., Beaulieu, J.-P., Yung, Y., Carey, S., Barber, R. J., Tennyson, J., Ribas, I., Allard, N., Ballester, G. E., Sing, D. K., & Selsis, F. 2007, *Nature*, 448, 169
- Triaud, A. H. M. J., Queloz, D., Bouchy, F., Moutou, C., Collier Cameron, A., Claret, A., Barge, P., Benz, W., Deleuil, M., Guillot, T., Hébrard, G., Lecavelier Des Étangs, A., Lovis, C., Mayor, M., Pepe, F., & Udry, S. 2009, *A&A*, 506, 377
- Werner, M. W. et al. 2004, *ApJS*, 154, 1
- Winn, J. N., Holman, M. J., Torres, G., McCullough, P., Johns-Krull, C., Latham, D. W., Shporer, A., Mazeh, T., Garcia-Melendo, E., Foote, C., Esquerdo, G., & Everett, M. 2008, *ApJ*, 683, 1076
- Winn, J. N., Johnson, J. A., Peek, K. M. G., Marcy, G. W., Bakos, G. Á., Enya, K., Narita, N., Suto, Y., Turner, E. L., & Vogt, S. S. 2007, *ApJ*, 665, L167



## A. SYSTEM PARAMETERS

TABLE 10  
SYSTEM PARAMETERS OF WASP-14.

PARAMETER	VALUE	REFERENCE
Eclipse Parameters		
Eclipse Midpoint (BJD <sub>TDB</sub> ) (2010-03-18)	$2455274.6617 \pm 0.0007$	a
Eclipse Midpoint (BJD <sub>TDB</sub> ) (2009-03-18)	$2454908.9296 \pm 0.0011$	a
Eclipse Duration $t_{4-1}$ (hrs)	$2.58 \pm 0.03$	a
Transit depth, $(R_p/R_{star})^2$	$0.0102^{+0.0002}_{-0.0003}$	c
Ingress/Egress Time $t_{2-1}$ (hrs)	$0.291 \pm 0.007$	a
Orbital Parameters		
Orbital Period, $P$ (days)	$2.2437661 \pm 0.0000011$	b
Semimajor axis, $a$ (AU)	$0.036 \pm 0.001$	c
Transit Time (BJD <sub>TDB</sub> )	$2454827.06666 \pm 0.00024$	b
Orbital eccentricity, $e$	$0.087 \pm 0.002$	b
Argument of pericenter, $\omega$ (deg)	$-107.1 \pm 0.5$	b
Velocity semiamplitude, $K$ (ms <sup>-1</sup> )	$990.0 \pm 3$	b
Centre-of-mass velocity $\gamma$ (ms <sup>-1</sup> )	$-4987.9 \pm 1.6$	b
Stellar Parameters		
Spectral Type	F5V	c
Mass, $M_*$ ( $M_\odot$ )	$1.211^{+0.127}_{-0.122}$	c
Radius, $R_*$ ( $R_\odot$ )	$1.306^{+0.066}_{-0.073}$	c
Mean density, $\rho_*$ ( $\rho_\odot$ )	$0.542^{+0.079}_{-0.060}$	c
Effective temperature, $T_{eff}$ (K)	$6475 \pm 100$	c
Surface gravity, $\log g_*$ (cgs)	$4.287^{+0.043}_{-0.038}$	c
Projected rotation rate, $v_* \sin(i)$ (kms <sup>-1</sup> )	$4.9 \pm 1.0$	c
Metallicity [M/H] (dex)	$0.0 \pm 0.2$	c
Age (Gyr)	$\sim 0.5\text{-}1.0$	c
Distance (pc)	$160 \pm 20$	c
Lithium abundance, $\log N(\text{Li})$	$2.84 \pm 0.05$	c
Planetary Parameters		
Mass, $M_p$ ( $M_J$ )	$7.341^{+0.508}_{-0.496}$	c
Radius, $R_p$ ( $R_J$ )	$1.281^{+0.075}_{-0.082}$	c
Surface gravity, $\log g_p$ (cgs)	$4.010^{+0.049}_{-0.042}$	c
Mean density, $\rho_p$ (gcm <sup>-3</sup> )	4.6	c
Equilibrium temperature (A=0), $T_{eq}$ (K)	$1866.12^{+36.74}_{-47.09}$	c

a - our analyses (parameters derived using 3-joint fit, see Section 5.4),

b - our analyses (see Section 6)

c - Joshi et al. (2009),